THE GAS PRODUCTION RATE AND COMA STRUCTURE OF COMET C/1995 O1 (HALE-BOPP)

Jeffrey P. Morgenthaler (jpmorgen@alum.mit.edu) and Walter M. Harris
University of Wisconsin–Madison, Space Astronomy Laboratory, 1150 University Ave., Madison, WI 53706, USA

Frederick L. Roesler and Frank Scherb
University of Wisconsin–Madison, Department of Physics, 1150 University Ave., Madison, WI 53706

Christopher M. Anderson and Nathaniel E. Doane
University of Wisconsin–Madison, Department of Astronomy, 1150 University Ave., Madison, WI 53706

Ronald J. Oliversen
NASA/Goddard Space Flight Center, Code 681, Greenbelt, MD 20771, USA

Abstract. The University of Wisconsin–Madison and NASA–Goddard conducted a comprehensive multi-wavelength observing campaign of coma emissions from comet Hale-Bopp, including OH 3080 Å, [O I] 6300 Å, H_2O^+ 6158 Å, H Balmer-α 6563 Å, NH_2 6330 Å, [C I] 9850 Å CN 3879 Å, C_2 5141 Å, C_3 4062 Å, C I 1657 Å, and the UV and optical continua. In this work, we concentrate on the results of the H_2O daughter studies. Our wide-field OH 3080 Å measured flux agrees with other, similar observations and the expected value calculated from published water production rates using standard H_2O and OH photochemistry. However, the total [O I] 6300 Å flux determined spectroscopically over a similar field-of-view was a factor of $3-4$ higher than expected. Narrow-band [O I] images show this excess came from beyond the H_2O scale length, suggesting either a previously unknown source of [O I] or an error in the standard $OH+\nu \rightarrow O(^1D)+H$ branching ratio. The Hale-Bopp OH and [O I] distributions, both of which were imaged to cometocentric distances $> 1\times10^6$ km, were more spatially extended than those of comet Halley (after correcting for brightness differences), suggesting a higher bulk outflow velocity. Evidence of the driving mechanism for this outflow is found in the Hα line profile, which was narrower than in comet Halley (though likely because of opacity effects, not as narrow as predicted by Monte-Carlo models). This is consistent with greater collisional coupling between the suprathermal H photodissociation products and Hale-Bopp's dense coma. Presumably because of mass loading of the solar wind by ions and ions by the neutrals, the measured acceleration of H_2O^+ down the ion tail was much smaller than in comet Halley. Tailward extensions in the azimuthal distributions of OH 3080 Å, [O I], and [C I], as well as a Doppler asymmetry in the [O I] line profile, suggest ion-neutral coupling. While the tailward extension in the OH can be explained by increased neutral acceleration, the [O I] 6300 Å and [C I] 9850 Å emissions show 13% and $>$ 200% excesses in this direction (respectively), suggesting a non-negligible contribution from dissociative recombination of CO^+ and/or electron collisional excitation. Thus, models including the effects of photo- and collisional chemistry are necessary for the full interpretation of these data.

Keywords: Carbon monoxide, comets, C/1995 O1 (Hale-Bopp), dissociative recombination, electron collisional excitation, hydrogen Balmer$-\alpha$ coma, hydroxyl radical photodissociation, metastable oxygen coma, water photochemistry, water production rate

1. Introduction

One of the major goals of cometary studies is to find the relative abundances of materials in the nucleus in order to answer fundamental questions of the origin and evolution of comets and the Solar System. Until the detailed bulk properties of several comets are probed by space craft visits, we must rely on remote sensing studies of the comet nucleus surface, coma, and dust to determine relative abundances. The scheme for using remote sensing studies to derive cometary abundance ratios goes something like this:

- Count all the photons produced in a few key coma emission lines
- Understand how these photons relate to parent populations
- Understand how outgassing rates relate to intrinsic nuclear abundance ratios
- Derive abundance ratios

Spectroscopy and narrow-band imaging are the tools used for isolating coma lines. Because most telescopes have narrow fields of view (FOVs) compared to the typical cometary coma, full interpretation of the data depends on models of the comet atmosphere and coma emissions. The smaller the telescope FOV, the more tenuous the connection between the measured flux and the intrinsic production rate of the target species (e.g., Cochran and Schleicher, 1993).

For three decades, the University of Wisconsin–Madison has specialized in using Fabry-Pérot (FP) spectrometers for sensitive studies of faint, diffuse emissions from the Earth's atmosphere, objects in the solar system, including comets and the Io plasma torus, and the Galaxy (e.g., Nossal et al., 2001; Magee-Sauer et al., 1988; Woodward et al., 1994; Reynolds, 2002). FPs have the advantage of providing very high spectral resolution and sensitivity with a very wide FOV (Roesler et al., 1995). FPs can be used as tuneable narrow-band filters for imaging applications (e.g., fig. 2) or for wide-field spectroscopy (e.g., Morgenthaler et al., ????, these proceedings). Thus, they are an excellent tool for measuring coma emissions. FP data can be used to constrain the models needed to relate coma emissions to parent populations and the models needed for the interpretation of data collected with more conventional observation techniques.

In most cometary atmospheres, interactions with the solar wind and radiation field are the dominant mechanisms for shaping the coma: collisions between atmospheric constituents in typical comets only occur within a few $\times 10^3$ km of the nucleus (Whipple and Huebner, 1976). Comet C/1995 O1 (Hale-Bopp) was not typical. With a water production rate, $Q(H_2O) > 1 \times$

10^{31} molecules s^{-1}, at perihelion, Hale-Bopp's collision sphere extended to $r \sim 10^5$ km (Combi et al., 1999; Harris et al., ????, these proceedings), which is comparable to the photodissociation scale length of H_2O at 1 AU. Thus, rather than simple Haser (1957) or vectorial (Festou, 1981) models, in most cases, sophisticated hydrodynamic or Monte-Carlo models (e.g., Crifo and Rodionov, 1999; Combi and Smyth, 1988) are needed to fully interpret Hale-Bopp's coma emissions.

Our collaborative team from the University of Wisconsin–Madison and NASA–Goddard conducted a comprehensive ground-based study of Hale-Bopp during its perihelion passage with the goal of mapping the intensity distributions and spectral line shapes of several species, notably H_2O daughters and $C(^1D)$. In this work, we briefly summarize all of the observations and results to date.

2. Observations

Nine instruments on eight telescopes were used in the Wisconsin/GSFC observing campaign. Table I shows which telescopes each instrument was coupled to. Several of the telescopes were located on Kitt Peak, including the 0.6 m siderostat and 150 mm FP imaging spectrometer that comprise the Wisconsin Hα Mapper (WHAM; Tufte, 1997), the McMath-Pierce (MMP) solar, Wisconsin Indiana, Yale, NRAO (WIYN), and Burrell Schmidt telescopes. The Halfwave Polarimeter (HPOL), an imaging spectropolarimeter (see, e.g., Meyer et al., 2002), was located at the Pine Bluff Observatory (PBO) in Pine Bluff, Wisconsin and the ADOPT adaptive optics imager was coupled to the 100″ Hooker telescope at Mt. Wilson. The Wide-field Imaging Survey Polarimeter (WISP) is a UV sounding rocket payload which was flown from White Sands Missile Range on 1997 April 8. As indicated in Table II, WISP recorded spectropolarimetric images of Hale-Bopp in C I 1657 Å and the UV continuum at 2700 Å. The configuration of this instrument and the results of these observations are presented by Harris et al. (1999). Images of Hale-Bopp were recorded by the Burrell Schmidt and Hooker 100″ telescopes using the narrow-band filters indicated in Tables II–III on the dates indicated in Figure 1. The Burrell had a 1° FOV and imaged the full spatial extent the species observed; the ADOPT system had a 22″ FOV and captured the detailed structure of the inner coma. Both the Densepak and Hydra MOSs were used to observe Hale-Bopp over a 300 Å bandpass centered on 6250 Å. The Densepak MOS is a hexagonal array of ninety-one 3″ fibers on 4″ centers. The Hydra MOS has ninety-six fibers, each with a 3″ FOV which can be arranged with very few constraints within a 1°diameter FOV. For these observations, Hydra was configured with the fibers in concentric rings centered on the nucleus, as indicated in Figure 2.

Table I. Wisconsin/GSFC Key to Instruments and Telescopes

Instrument	Telescope
WISP (UV imaging polarimeter)	0.3 m sounding rocket 36.157 UL
Burrell Schmidt (wide-field imager)	0.6 m Schmidt, Kitt Peak
WIYN MOS (Hydra and Densepak MOS)	3.5 m WIYN, Kitt Peak
WHAM FP (imager/spectrometer)	0.6 m Wisconsin Hα Mapper, Kitt Peak
MMP 150 mm FP (imager)	0.9 m McMath-Pierce West Auxiliary
MMP 50 mm FP (spectrometer)	2.0 m McMath-Pierce Main, North Port
PBO HPOL (imaging spectropolarimeter)	0.9 m Pine Bluff Observatory
ADOPT (adaptive optics imager)	2.5 m (100″) Hooker, Mt. Wilson

Table II. Wisconsin/GSFC Key to Observations

Instrument	Emission Source	λ (Å)	R[1]
WISP	C I	1657 ± 50	
WISP	UV Continuum	2700 ± 35	
Burrell Schmidt	CN, C_2, C_3,		
	OH, Cont. (blue, green)	Table III	
Hooker 100″ ADOPT	CN, C_2, H_2O^+,		
	Cont. (blue), R-band	Table III	
WIYN MOS	H_2O^+, NH_2, [O I], C_2	6100–6400	15,000
WHAM 150 mm FP	[O I]	6300	25,000[2]
WHAM 150 mm FP	H_2O^+	6170	25,000[2]
MMP 150 mm FP	H_2O^+	6158	15,000
MMP 50 mm FP	[O I]	6300	60,000
MMP 50 mm FP	Hα	6563	60,000
MMP 50 mm FP	[C I]	9850	40,000
PBO HPOL	Continuum	3200–10,500	500

[1] resolving power ($\lambda/\Delta\lambda$)
[2] imaging and spectral capabilities

We operated the three FPs in one of two modes: imaging or spectroscopic. In the first case, the sky is imaged onto a CCD camera through the FP. An iris can be used to adjust the bandpass of the image, from the free spectral range of the instrument down to the intrinsic resolving power. The central wavelength of the image can be adjusted to a precision much better than the intrinsic resolving power of the instrument. In spectral mode, the FP ring pattern is imaged directly onto the CCD, capturing the entire free spectral range of the instrument in one exposure. Although changing between imaging and spectral mode is a simple matter of inserting or removing lenses, we

Table III. Filter Specifications

Filter	λ^1
OH	3090 ± 31
CN	3870 ± 31
C_3	4062 ± 31
Blue Cont.	4450 ± 33
C_2	5141 ± 59
Green Cont.	5260 ± 28
R-band	6450 ± 700
H_2O^+	7020 ± 85

[1] center $\pm$ bandpass (Å)

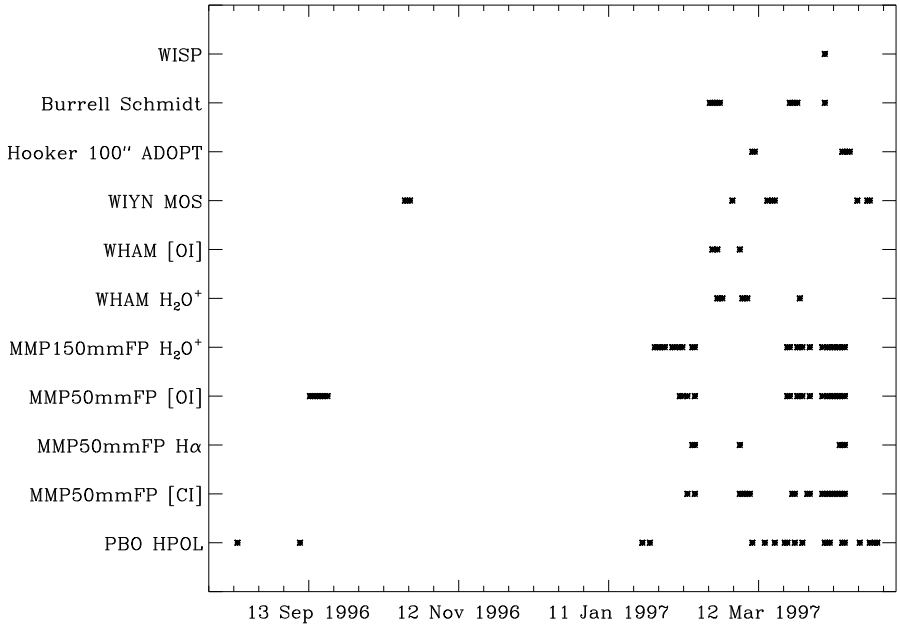

Figure 1. Summary of Wisconsin/NASA–GSFC comet Hale-Bopp observations.

recorded data with the 150 mm FP on the MMP only in image mode and the 50 mm FP only in spectral mode. WHAM data was recorded in both modes.

3. Data Reduction

The Burrell Schmidt OH images, WHAM [O I] spectra and images, the WISP UV images, and most of the WIYN MOS spectra have been fully

and optimally reduced. The results of the WIYN MOS NH_2 analyses are reported elsewhere (Glinski et al., 2001). The $H\alpha$, [C I], and [O I] spectra from the 50 mm FP at the McMath-Pierce telescope are fully reduced, though refinements in these reductions discussed by Morgenthaler et al. (????, these proceedings) may lead to more stable surface brightness values and, in the case of $H\alpha$, detailed line shapes. The HPOL data have been reduced by pipeline software, which merges the entire $1'$ FOV. Extracting the spatially varying components of the dust polarization as a function of wavelength within that $1'$ FOV requires software that has yet to be developed. The narrow-band filter images taken at Mt. Wilson have been preliminarily reduced and show structure similar to that seen by other observers, but we are unsure of the effect of the diffuse nature of Hale-Bopp's inner coma on the ADOPT system and the resulting image quality. None of the WHAM H_2O^+ data and only one night of the McMath-Pierce 150 mm FP H_2O^+ data have been reduced. Similarly, except for OH, the narrow-band filter images taken with the Burrell Schmidt telescope remain unreduced.

4. Results

4.1. OH AND $O(^1D)$

The Burrell Schmidt OH images and the WHAM [O I] spectra were taken over a sufficiently large FOV (1°, or 1×10^6 km for Hale-Bopp at perihelion) that essentially all the emission from these species was detected. Using the OH 3080 Å g-factor, Harris et al. (????, these proceedings) find OH production rates, Q(OH), consistent with other results. Using standard H_2O and OH photochemistry, Harris et al. convert these Q(OH) values into Q(H_2O) values that also agree with other results (e.g., Combi et al., 2000). Using the Combi et al. Q(H_2O) values and standard H_2O and OH photochemistry (Huebner et al., 1992; van Dishoeck and Dalgarno, 1984), [O I] spectra from four instruments on three telescopes taken over the span of two months show evidence of $3-4$ times more [O I] emission than expected (Morgenthaler et al., 2001). Morgenthaler et al. (2001) present radial profiles of the WHAM [O I] image shown in Figure 2 from regions excluding the tailward extension (discussed in §4.5) to demonstrate that this excess came from beyond the H_2O scale length. This suggests either a previously unknown source of $O(^1D)$ or an error in the $OH + \nu \rightarrow O(^1D) + H$ branching ratio of van Dishoeck and Dalgarno (1984). Using the experimentally determined OH photodissociation cross section at Lyα of Nee and Lee (1984) as a guide, Morgenthaler et al. propose a modification to the OH cross section that predicts the observed [O I] without undue modification to the total OH photodissociation lifetime. Because of differing excess energies of photodissociation, modification of

the branching ratio implies a change in the Hα line shape which may be detectable in our Hα data (§4.2).

4.2. Hα

As described by Morgenthaler et al. (????, these proceedings), we measure Hale-Bopp's Hα line width to be $11 - 13$ km s^{-1} (FWHM) for a $\sim 2.7 \times 10^5$ km FOV centered $\sim 3.3 \times 10^5$ km sunward of the nucleus. This is significantly broader than the intrinsic line width of 4.5 km s^{-1} predicted by Monte-Carlo techniques (Combi, 2002, private communication). Opacity in the Hα line is likely the reason for this discrepancy. As shown by Smyth et al. (1993), the Hα line profiles predicted by these Monte-Carlo simulations are quite complicated; H atoms are produced in photodissociation events with a variety of excess energies and are thermalized with varying efficiencies, depending on the local coma density. The 5 km s^{-1} resolution of our Hale-Bopp Hα measurements is sufficient to reveal some of this predicted structure and may be useful in testing the hypothesis posed by Morgenthaler et al. (2001), that the van Dishoeck and Dalgarno (1984) OH + $\nu \rightarrow$ O(^1D) + H branching ratio may be too low (§4.1).

4.3. [C I] 9850 Å

Because of Hale-Bopp's high production rate and resulting brightness, many emission lines previously undetected or marginally detected in comets were observed and studied in detail. The first ground-based detection of cometary [C I] emission was reported by Münch et al. to the International Halley Watch hotline (Tozzi et al., 1998). Oliversen et al. (2002) were able to obtain quantitative [C I] emission measurements on 11 nights, including measurements off the nucleus in the sunward and anti-sunward directions. Oliversen et al. find a factor two more [C I] emission tailward compared to sunward for $\sim 2.7 \times 10^5$ km diameter FOVs centered at cometocentric radii of $\sim 3.4 \times 10^5$ km. The emission observed in the tailward direction is roughly consistent with a photodissociation model but since the distribution of other species show tailward extensions rather than sunward deficits, Oliversen et al. propose that the spatial distribution of [C I] is primarily determined by effects other than photodissociation. For instance, dissociative recombination of CO^+ was cited as the major source of [C I] 1931 Å emission in comet C/1975 V1-A (West; Feldman, 1978). As discussed in §4.5, electron collisional excitation of C is also a possible mechanism. As a result of these effects, even with the relatively large FOV (4′.1) of the 50 mm FP, it is not possible to simply invert the [C I] flux values to obtain an estimate of Q(CO), as done for [O I] and Q(H_2O). Rather, a sophisticated global coma model is needed to describe the complex photo- and collisional chemistry of the neutrals and ions as a function of position in the coma.

4.4. H_2O^+ Velocity Distribution

Preliminary analysis of the MOS data (Anderson, 1999) shows that the acceleration of H_2O^+ down the tail of Hale-Bopp was 16–19 cm s^{-2} compared to 30–300 cm s^{-2} in Halley (Scherb et al., 1990). This suggests that mass loading of the the solar wind and/or collisions between the ions and neutrals play a more important role in Hale-Bopp than Halley. Using velocity resolved H_2O^+ images recorded with WHAM and the 150 mm FP at the McMath-Pierce telescope, we expect to map the coma ion velocity distribution on up to 20 nights between 1997 Jan 30 and Apr 16. These maps will constrain global models of the neutral/ion interactions and may provide a clue to the cause of the asymmetries seen in our OH, [O I] 6300 Å, and [C I] 9850 Å data (§4.5).

4.5. Tailward Asymmetry

The OH 3080 Å, [O I] 6300 Å, and [C I] 9850 Å data show extensions in the tailward direction. Harris et al. (2002, ????, these proceedings) show that in OH, this extension lies somewhere between the ion and dust tails. Harris et al. argue that the total amount of OH in this azimuthal slice of the coma is the same as in the other directions, but it is accelerated more than elsewhere, resulting in a lower surface brightness close to the nucleus and a higher surface brightness further away. Harris et al. suggest that collisions between ions and neutrals in Hale-Bopp's dense coma are responsible for both the low H_2O^+ acceleration (§4.4; Anderson, 1999) and the increased acceleration of OH in the anti-sunward direction.

Figures 2–3 show a similar result for the [O I] data. Furthermore the high resolution [O I] spectra recorded by the 50 mm FP over its 2′ radius FOV (centered on the nucleus) show red wings (Morgenthaler et al., 2001, fig. 4), which, given the viewing geometry, is consistent with $O(^1D)$ atoms flowing down the ion tail. This provides partial support for the ion collisional acceleration mechanism proposed by Harris et al. However, unlike the OH emission, the [O I] emission shows a 13% excess in the tailward quadrant. Because there is no excess OH emission, we can assume that there is no additional source of H_2O or OH in this region, and that the extra $O(^1D)$ is coming from some other source. The likely sources are: electron collisional excitation of O and dissociative recombination of oxygen-bearing species.

Support for electron collisional excitation of [O I] 6300 Å is provided by the detection of [O I] 1356 Å emission at cometocentric distances of 1.6×10^4 km (McPhate et al., 1999), since this transition is not excited by dissociation. Although collisional excitation cross sections are highly energy dependent, it is reasonable to assume a broad enough electron energy distribution in the coma so that collisional excitation of [O I] 6300 Å (and [C I] 9850 Å) is also implied. Support for dissociative recombination of

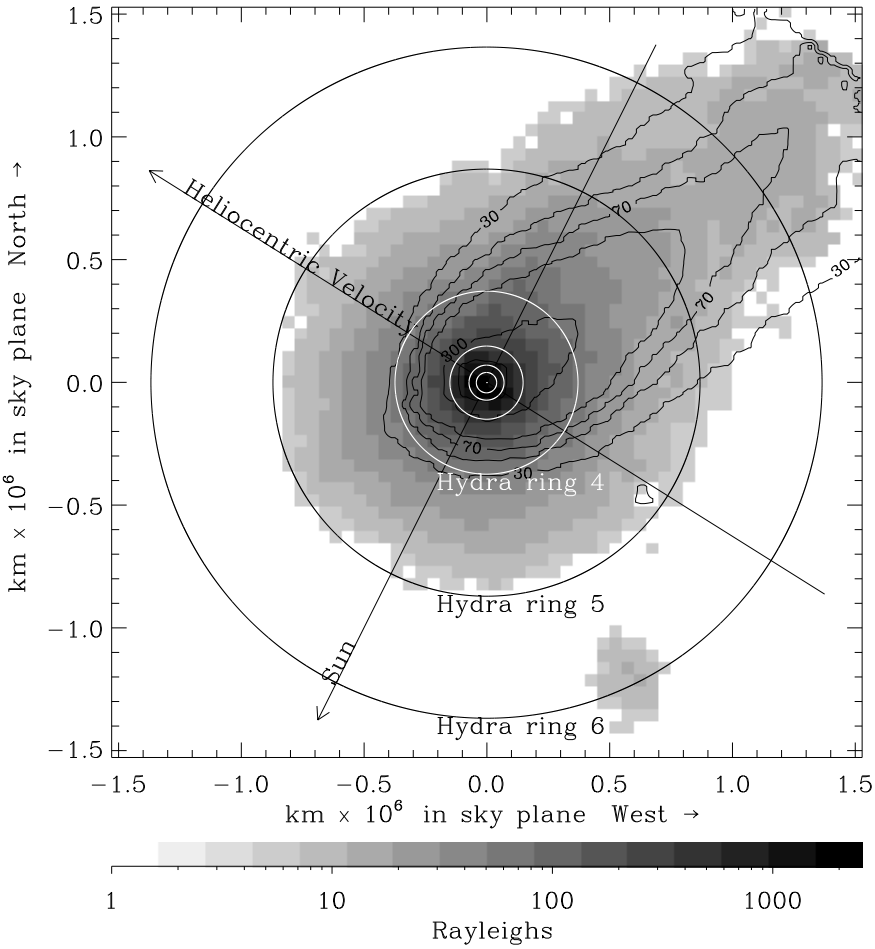

Figure 2. Hale-Bopp March 5 image with [O I] 6300 Å emission shown in gray scale, dust in contours, and circles showing positions of the Hydra annuli plotted in fig. 3. The edge of the 1° WHAM FOV can be seen in the dust contours in the upper right hand corner of the image. The angular radii of the Hydra rings are: 0′.67, 1′.15, 2′.4, 6′, 14′, and 22′.

CO^+ comes from the strong tailward asymmetry seen in our [C I] 9850 Å data (§4.3). This effect would also contribute to the tailward excess in the [O I] 6300 Å emission.

5. Conclusions

Particle densities in a cometary coma and dust tail span the range from near terrestrial atmospheric to interplanetary and are unperturbed by the gravitation of the nucleus. Thus, the coma and dust tail provide excellent laboratories

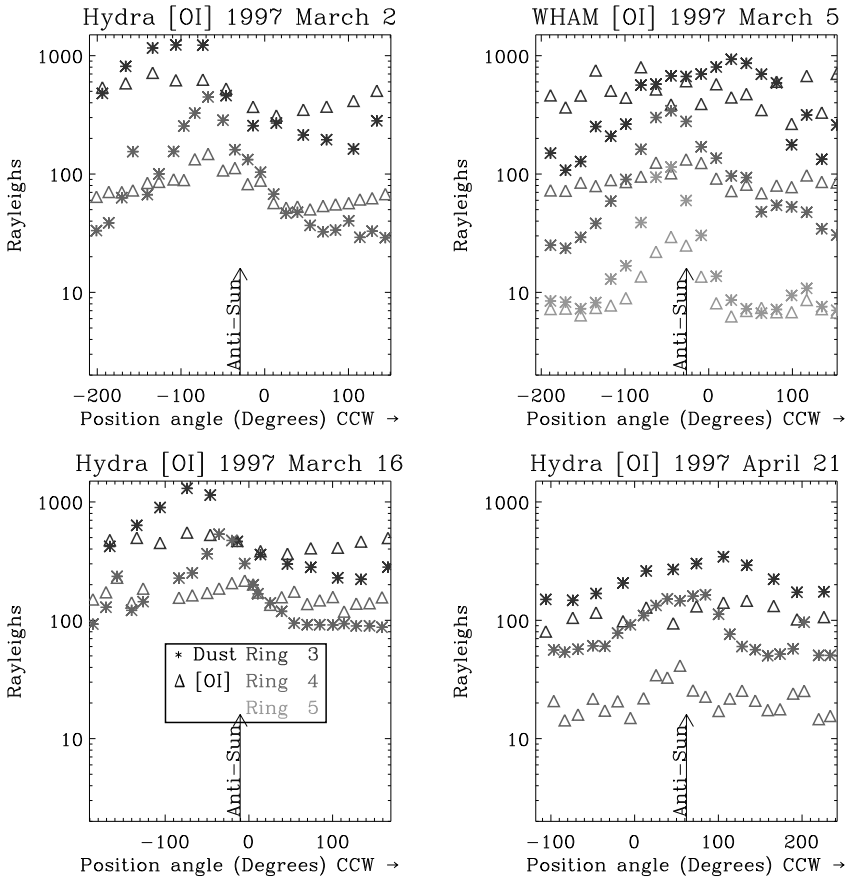

Figure 3. Comparison of the WHAM and Hydra [O I] data. The triangles show the azimuthal distribution of the [O I] surface brightness, the asterisks show the dust surface brightness. The Hydra surface brightness values are plotted directly, with the greyscale and legend indicating which ring in fig. 2 the data correspond to. The values for the points in the top right plot were derived from the WHAM image by dividing it into 5-pixel wide rings (1 pixel = 0.′8) centered on the Hydra rings and finding the average pixel value in 20 azimuthal bins.

for study of gas collisional chemistry, solar photochemistry, the solar wind, metastable state emissions, dust polarization, etc. For proper characterization of these effects, it is essential to observe diffuse coma emissions from the major cometary volatiles and their daughter products to distances beyond the photodissociation scale lengths of the emitting species. The high sensitivity, wide-field, narrow-band imaging and spectroscopic capabilities of Fabry-Pérot spectrometers used by the Wisconsin/GSFC team, complemented by conventional multi-object spectroscopy and narrow-band filter imaging provided the necessary set of data for studying detailed coma physics in Hale-Bopp. With a more complete understanding of cometary comæ, the funda-

mental questions of cometary composition and origin can be more accurately studied with remote sensing techniques.

References

Anderson, C. M.: 1999, *Earth, Moon, Planets* **78**, 99.

Cochran, A. L. and Schleicher, D. G.: 1993, *Icarus* **105**, 235–253.

Combi, M. R., Kabin, K., De Zeeuw, D. L., Gombosi, T. I., and Powell, K. G.: 1999, *Earth, Moon, Planets* **79**, 275–306.

Combi, M. R., Reinard, A. A., Bertaux, J., Quemerais, E., and Mäkinen, T.: 2000, *Icarus* **144**, 191–202.

Combi, M. R. and Smyth, W. H.: 1988, *ApJ* **327**, 1026–1043.

Crifo, J. F. and Rodionov, A. V.: 1999, *Planet. Space Sci.* **47**, 797–826.

Feldman, P. D.: 1978, *A&A* **70**, 547–553.

Festou, M. C.: 1981, *A&A* **95**, 69–79.

Glinski, R. J., Post, E. A., and Anderson, C. M.: 2001, *ApJ* **550**, 1131–1139.

Harris, W. M., Morgenthaler, J., Mierkiewicz, E., Scherb, F., Oliversen, R., and Nordsieck, K., ????, these proceedings.

Harris, W. M., Nordsieck, K. H., Scherb, F., and Mierkiewicz, E. J.: 1999, *Earth, Moon, Planets* **78**, 161–167.

Harris, W. M., Scherb, F., Mierkiewicz, E. J., Oliversen, R. J., and Morgenthaler, J. P.: 2002, *ApJ* **578**, 996–1008.

Haser, L.: 1957, *Bull. Soc. Roy. Sci. Liège* **43**, 740.

Huebner, W. F., Keady, J. J., and Lyon, S. P.: 1992, *Astrophys. Space Sci.* **195**, 1–294.

Magee-Sauer, K., Roesler, F. L., Scherb, F., Harlander, J., and Oliversen, R. J.: 1988, *Icarus* **76**, 89–99.

McPhate, J. B., Feldman, P. D., McCandliss, S. R., and Burgh, E. B.: 1999, *ApJ* **521**, 920–927.

Meyer, J. M., Nordsieck, K. H., and Hoffman, J. L.: 2002, *AJ* **123**, 1639–1646.

Morgenthaler, J. P., Harris, W. M., Scherb, F., Anderson, C. M., Oliversen, R. J., Doane, N. E., Combi, M. R., Marconi, M. L., and Smyth, W. H.: 2001, *ApJ* **563**, 451–461.

Morgenthaler, J. P., Harris, W. M., Scherb, F., and Oliversen, R. J., ????, these proceedings.

Nee, J. B. and Lee, L. C.: 1984, *J. Chem. Phys.* **81**, 31–36.

Nossal, S., Roesler, F. L., Bishop, J., Reynolds, R. J., Haffner, M., Tufte, S., Percival, J., and Mierkiewicz, E. J.: 2001, *J. Geophys. Res.* **106**, 5605–5616.

Oliversen, R. J., Doane, N. E., Scherb, F., Harris, W. M., and Morgenthaler, J. P.: 2002, *ApJ* **581**. in press.

Reynolds, R. J.: 2002, *Scientific American* **286**, 32–41.

Roesler, F. L., Reynolds, R. J., and Scherb, F.: 1995, in *Tridimensional Optical Spectroscopic Methods in Astrophysics*, pp. 95–106, ASP.

Scherb, F., Magee-Sauer, K., Roesler, F. L., and Harlander, J.: 1990, *Icarus* **86**, 172–188.

Smyth, W. H., Marconi, M. L., Scherb, F., and Roesler, F.: 1993, *ApJ* **413**, 756–763.

Tozzi, G. P., Feldman, P. D., and Festou, M. C.: 1998, *A&A* **330**, 753–763.

Tufte, S. L.: 1997, 'The WHAM spectrometer, design, performance characteristics and first results'. Ph.D. thesis, University of Wisconsin–Madison.

van Dishoeck, E. F. and Dalgarno, A.: 1984, *Icarus* **59**, 305–313.

Whipple, F. L. and Huebner, W. F.: 1976, *ARA&A* **14**, 143–172.

Woodward, R. C. J., Scherb, F., and Roesler, F. L.: 1994, *Icarus* **111**, 45–64.